



Article

Sodium Alginate/UiO-66-NH₂ Nanocomposite for Phosphate Removal

Xiaohang Lin, Yuzhu Xiong  and Fuping Dong * 

Department of Polymer Materials and Engineering, College of Materials and Metallurgy, Guizhou University, Guiyang 550025, China; 18185070974@163.com (X.L.); yzxiong@gzu.edu.cn (Y.X.)

* Correspondence: fpdong@gzu.edu.cn; Tel.: +86-155-1903-7121

Abstract: Environmental pollution of phosphorus is becoming increasingly concerning, and phosphate removal from water has become an important issue for controlling eutrophication. Modified metal–organic framework (MOF) materials, such as UiO-66-NH₂, are promising adsorbents for phosphate removal in aquatic environments due to their high specific surface area, high porosity, and open active metal sites. In this study, a millimeter-sized alginate/UiO-66-NH₂ composite hydrogel modified by polyethyleneimine (UiO-66-NH₂/SA@PEI) was prepared. The entrapping of UiO-66-NH₂ in the alginate microspheres and its modification with PEI facilitate easy separation in addition to enhanced adsorption properties. The materials were characterized by SEM, FTIR, XRD, and BET. Static, dynamic, and cyclic adsorption experiments were conducted under different pH, temperature, adsorbent dosage, and initial concentration conditions to assess the phosphate adsorption ability of UiO-66-NH₂/SA@PEI. Under optimal conditions of 65 °C and pH = 2, 0.05 g UiO-66-NH₂/SA@PEI adsorbed 68.75 mg/g, and the adsorption rate remained at 99% after five cycles of UiO-66-NH₂/SA@PEI. These results suggest that UiO-66-NH₂/SA@PEI composite materials can be used as an effective adsorbent for phosphate removal from wastewater.

Keywords: sodium alginate; UiO-66-NH₂; phosphate removal; porous nanocomposite



Citation: Lin, X.; Xiong, Y.; Dong, F. Sodium Alginate/UiO-66-NH₂ Nanocomposite for Phosphate Removal. *Nanomaterials* **2024**, *14*, 1176. <https://doi.org/10.3390/nano14141176>

Academic Editor: Yannick Guari

Received: 31 May 2024

Revised: 1 July 2024

Accepted: 9 July 2024

Published: 10 July 2024



Copyright: © 2024 by the authors. Licensee MDPI, Basel, Switzerland. This article is an open access article distributed under the terms and conditions of the Creative Commons Attribution (CC BY) license (<https://creativecommons.org/licenses/by/4.0/>).

1. Introduction

Phosphorus pollution resulting from the extensive production and mismanagement of pesticides, detergents, and phosphate fertilizers is becoming more and more serious [1]. Phosphorus manifests in water bodies in multiple forms, such as phosphates, polyphosphates, and organic phosphorus. Excessive phosphate in water can cause eutrophication, leading to the growth of harmful blue-green algae, water quality decline, abnormal death of fish/invertebrates, and ultimately disturbing the local ecological balance, causing harm to the ecological environment [2]. The removal of phosphate from water bodies is essential to enhance the ecological environment [3].

Various methods, such as precipitation, adsorption, ion exchange, and biological processes have been utilized to remediate phosphate pollution [4–8]. Phosphorus, a non-renewable resource, is significant not only for preventing phosphorus pollution but also for recycling phosphorus resources from wastewater [9]. The adsorption method facilitates the dual purpose of removing contaminants from water bodies and converting them into fertilizer for agricultural use. The development of efficient adsorbents and techniques for phosphate removal holds significant practical importance for the protection of water resources and the environment [10].

In the adsorption of phosphate in wastewater, the oxides and hydroxides of trivalent and tetravalent metals like Fe, Al, Mn, La, Ce, and Zr demonstrate rapid kinetics and superior adsorption capacity [11]. Metal–organic frameworks (MOFs) have recently attracted significant attention for their potential in phosphate removal applications. With high surface areas, controllable pore dimensions, substantial porosity, unique architecture, diverse

functional groups, and stability under varying temperature and pH conditions, MOFs are well suited as adsorbents for phosphate recovery compared to conventional oxides and hydroxides [12]. In fact, MOFs have exhibited enhanced phosphate adsorption capabilities when constructed using appropriate metal and organic ligands, which are attributed to their superior specific surface areas and stability [13–17]. Shams et al. developed a novel hybrid adsorbent, cubic zeolitic imidazolate framework-8 (ZIF-8), and assessed its efficacy in removing phosphate from aqueous solutions, revealing a notable adsorption capacity of 38.22 mg/g [18]. Zirconium-based MOFs, compared to other metals, exhibit ordered porous structures, diverse functional groups, excellent ion exchange/adsorption capabilities, and outstanding water stability [19–23]. Consequently, they are being investigated for phosphate adsorption and removal in water.

However, the particle agglomeration of MOFs often causes a lack of full contact between the active adsorption sites and the adsorbate, ultimately limiting the adsorption efficiency of the materials [24]. MOFs typically exist in powder form, posing challenges for their recyclability after being utilized for phosphate adsorption [25,26]. Sodium alginate (SA), a natural and cheap polysaccharide polymer, has a strong ability to bond with multivalent metal ions in aqueous solutions, and it forms a stable hydrogel by cross-linking [27–30]. In this study, UiO-66-NH₂ nanoparticles were compounded with sodium alginate, gelled with Ca²⁺, surface grafted with polyethyleneimine, and subsequently exchanged with Zr⁴⁺ to produce UiO-66-NH₂/SA@PEI composites. The impact of pH, temperature, adsorbent dosage, and initial concentration on phosphate removal using the composite material was systematically investigated through batch experiments, with a discussion on its static/dynamic adsorption and regeneration performance.

2. Materials and Methods

2.1. Chemicals

Sodium alginate, zirconium oxychloride octahydrate (99%), polyethylene imine (PEI, M_w = 10,000, 99%), glacial acetic acid (99.5%), N, N-dimethylformamide (99.5%), zirconium chloride (98%), ammonium molybdate (99.8%), potassium antimony tartrate hemihydrate (98%), and potassium dihydrogen phosphate (99.5%) were purchased from Aladdin, Shanghai, China; anhydrous calcium chloride was obtained from Xilong Chemical, Shantou, China; 2-Amino para benzyl dimethyl (98%) and L-ascorbic acid (>99.0%) were acquired from Macklin, Shanghai, China; sulfuric acid and hydrochloric acid were purchased from Chuandong Chemical, Chongqing, China; and sodium hydroxide (AR) was obtained from Chengdu Jinshan Chemical Reagent Company (Chengdu, China). Deionized water (DW) was produced by an ultra-pure water instrument.

2.2. Synthesis of UiO-66-NH₂/SA@PEI

UiO-66-NH₂ nanoparticles were prepared according to the previous literature [31]. To synthesize UiO-66-NH₂/SA, 1.5 g of UiO-66-NH₂ was dispersed in 50 mL of water, followed by the addition of 1 g of sodium alginate after ultrasonication. The resulting mixture was heated at 100 °C in a water bath and stirred for 12 h to form a viscous suspension. This suspension was then slowly added dropwise into a 5% (*w/v*) CaCl₂ solution and allowed to react for 12 h with gentle stirring to form hydrogel beads. Subsequently, the beads underwent three water washes to remove residual CaCl₂, followed by immersion in a 2% polyethyleneimine 10000 (PEI-10000) solution at 50 °C for 1 h, and then rinsed with water. Finally, the hydrogel beads were immersed in a 50 mL ZrOCl₂ aqueous solution (5% wt) for 12 h to displace the calcium ions within the beads, followed by three water washes and freeze-drying for preservation.

2.3. Adsorption of Phosphate by UiO-66-NH₂/SA@PEI

The content of phosphate in the solution was determined by molybdenum antimony anti-spectrophotometry. An appropriate amount of UiO-66-NH₂/SA@PEI was added to 25 mL of a phosphate solution whose pH had been adjusted with NaOH and HCl.

Following this, an adsorption experiment was conducted at a predetermined temperature. Subsequently, the adsorption capacity of UiO-66-NH₂/SA@PEI could be calculated with Formulas (1) and (2).

$$Q_e = \frac{(C_0 - C_e) \cdot V}{M} \quad (1)$$

$$\text{Removal rate \%} = \frac{C_0 - C_t}{C_0} \times 100\% \quad (2)$$

Q_e is the equilibrium adsorption capacity of UiO-66-NH₂/SA@PEI, mg/g; C_0 is the initial concentration of phosphate solution, mg/L; C_e is the concentration of phosphate solution at equilibrium, mg/L; V is the solution volume, mL; and M is the mass of the adsorbent, g.

For recycling adsorption, UiO-66-NH₂/SA@PEI was immersed in a 0.1 M NaOH solution for 30 min and then washed with water for further adsorption experiments.

A dynamic adsorption system of UiO-66-NH₂/SA@PEI was designed with a peristaltic pump and glass beads, allowing the liquid to enter and exit the column from the bottom. The adsorption column had an inner diameter of 1 cm and a length of 20 cm, with the adsorbent positioned in the middle and glass beads filling the top and bottom. The adsorption efficiency of the UiO-66-NH₂/SA@PEI sample was studied under different concentrations of phosphate solutions and peristaltic pump flow rates.

2.4. Characterizations

The morphology of the adsorbent was observed by scanning electron microscopy (SEM) using an FEI-SEM system (FEI Helios Nanolab 600i, Hillsboro, OR, USA) operating at 15 kV. Before measurement, all samples were sprayed with a thin gold film. Fourier transform infrared spectroscopy (FTIR) was recorded on a Perkin-Elmer Spectrum GX-spectrophotometer (Waltham, MA, USA) with a spectral resolution of 1 cm⁻¹ and a scan number of 32. X-ray diffraction (XRD) patterns were recorded using a Philips diffractometer with a Geiger counter (Eindhoven, The Netherlands). The X-ray tube was operated at 40 kV and 30 mA (Cu K α radiation with Ni filter, $\lambda = 1.5406 \text{ \AA}$) with a scan speed of 1°/min. Nitrogen adsorption-desorption measurements (ASAP 2046, Micromeritics, Norcross, GA, USA) were performed at 77 K to assess their Brunauer-Emmett Teller (BET) surface areas. UV-visible spectra were recorded using a UV-2700 spectrophotometer (Shimadzu, Kyoto, Japan) with 1 cm quartz cuvettes.

3. Results

3.1. Characterization

The morphology of the material was analyzed using a scanning electron microscope before and after the phosphate adsorption. The results revealed no significant differences in size or morphology and only a slight increase in surface roughness (Figure 1a,b). Examination of the cross-section images showed that the structure of the adsorbent remained intact after the phosphate adsorption (Figure 1c,d). Furthermore, a close connection between the UiO-66-NH₂ nanoparticles and the SA network structure was observed.

Figure 2 shows the FT-IR spectra of the SA, UiO-66-NH₂, SA@PEI and UiO-66-NH₂/SA@PE materials before and after the adsorption. It can be observed that the stretching vibration peak of -OH in SA appeared at 3430 cm⁻¹, while the stretching vibration of -CH₂ occurred at 2930 cm⁻¹. Furthermore, the absorption peaks at 1638 cm⁻¹ and 1410 cm⁻¹ were attributed to the stretching vibration of -COOH [32]. Additionally, the absorption peak at 1031 cm⁻¹ was caused by the stretching vibration of -COC. After the PEI was grafted, the peak position at 3000–3500 cm⁻¹ shifted to the right, and the peak value was enhanced, indicating an increase in the NH₂ groups [33]. The FTIR spectrum of UiO-66-NH₂/SA@PEI displayed the characteristic peaks of UiO-66-NH₂ at various positions, which suggests that UiO-66-NH₂/SA was successfully compounded. A comparison between Figures 2c and 2d reveals a significant enhancement of the peak at 1047 cm⁻¹,

with the absorption peak region for the P-O stretching vibrations located between 1000 and 1100 cm^{-1} , indicating successful phosphate adsorption [34].

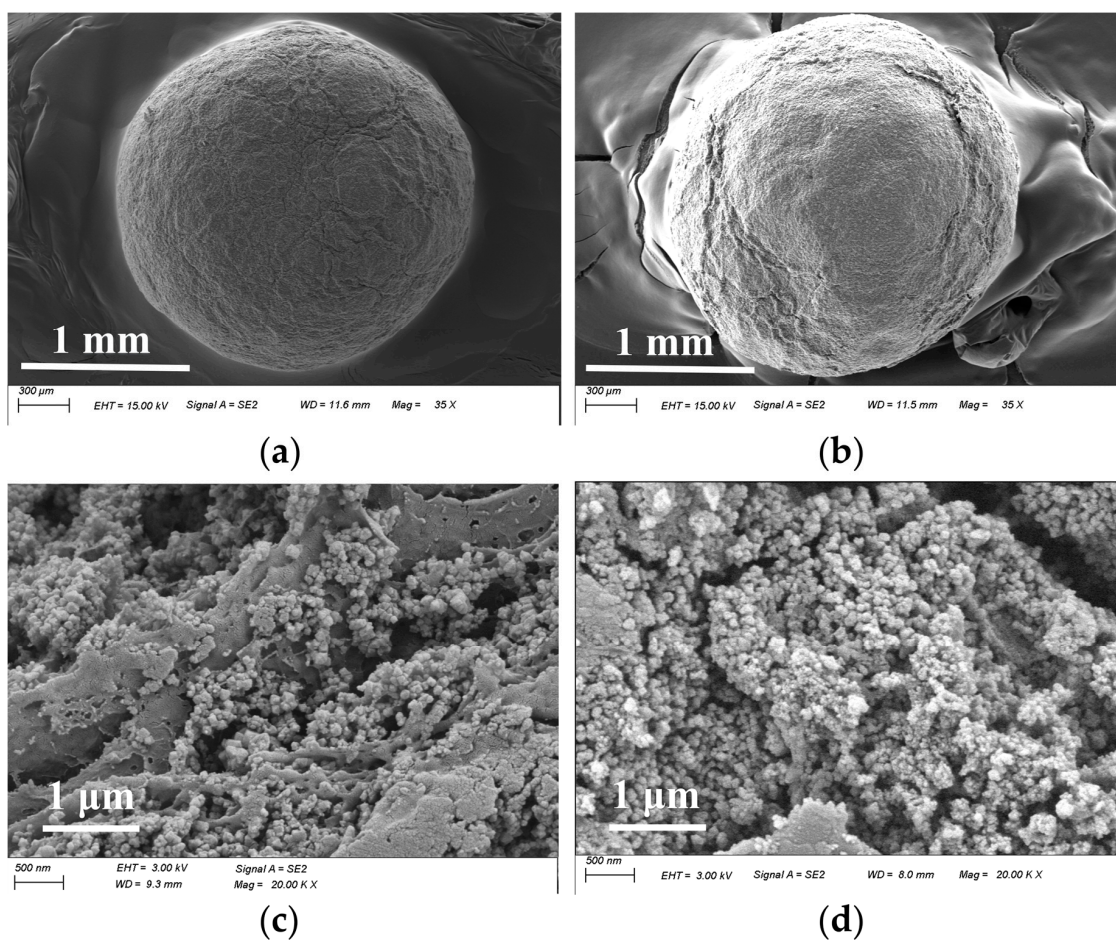


Figure 1. The SEM images of UiO-66-NH₂/SA@PEI before (a,c) and after the phosphate adsorption (b,d).

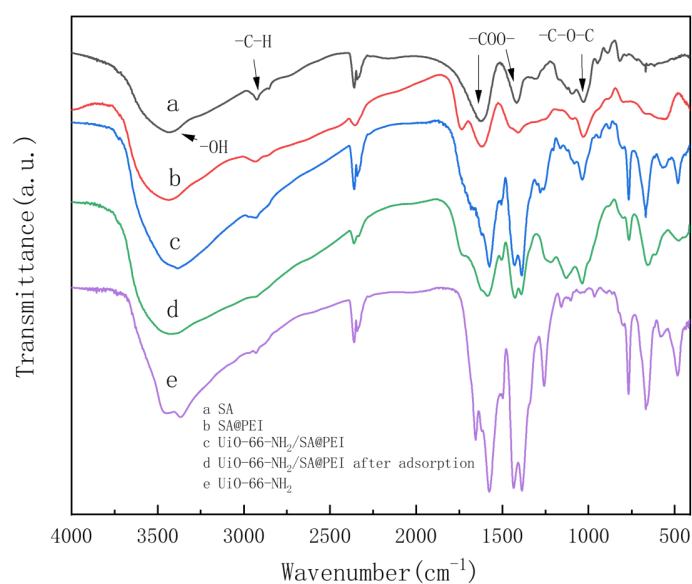


Figure 2. FTIR spectra of (a) SA, (b) SA@PEI, (c,d) UiO-66-NH₂/SA@PEI before and after adsorption, (e) UiO-66-NH₂.

The adsorption–desorption isotherms and pore size distribution curves of UiO-66-NH₂ and UiO-66-NH₂/SA@PEI are shown in Figure 3a,b. The N₂ adsorption–desorption isotherm of UiO-66-NH₂ exhibited a Type II curve. Upon composite formation with SA@PEI, UiO-66-NH₂/SA@PEI displayed a distinct hysteresis loop in the P/P₀ range of 0.6–1.0. The specific surface area decreased from 1062.2 m²/g to 325.1 m²/g, while the pore volume reduced from 0.5 cm³/g to 0.3 cm³/g. Furthermore, the average pore diameter increased from 1.9 nm to 3.7 nm, facilitating enhanced diffusion of phosphates within the material and providing additional adsorption sites for potential applications.

Figure 4 illustrates that UiO-66-NH₂ exhibited strong characteristic peaks at 7.35°, 8.45°, and 25.7°, while SA@PEI had weaker peaks at 13.63° and 21.31° [35]. The spectrum for UiO-66-NH₂/SA@PEI revealed that the characteristic peaks of UiO-66-NH₂ remained intact, indicating that the combination of sodium alginate did not change the crystal structure of UiO-66-NH₂.

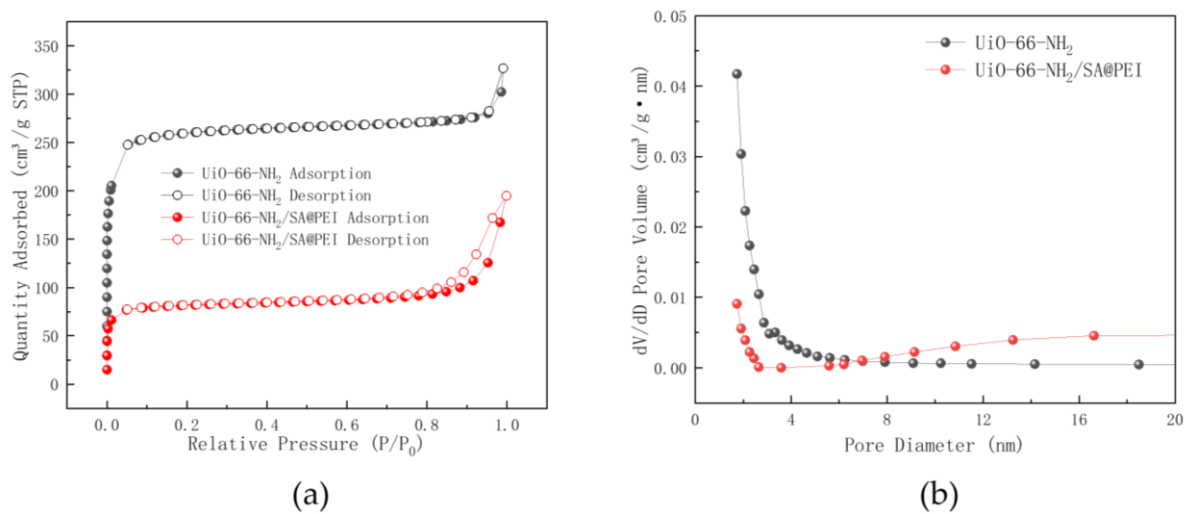


Figure 3. (a) N₂ adsorption–desorption isotherms and (b) pore size distribution curves for UiO-66-NH₂ and UiO-66-NH₂/SA@PEI.

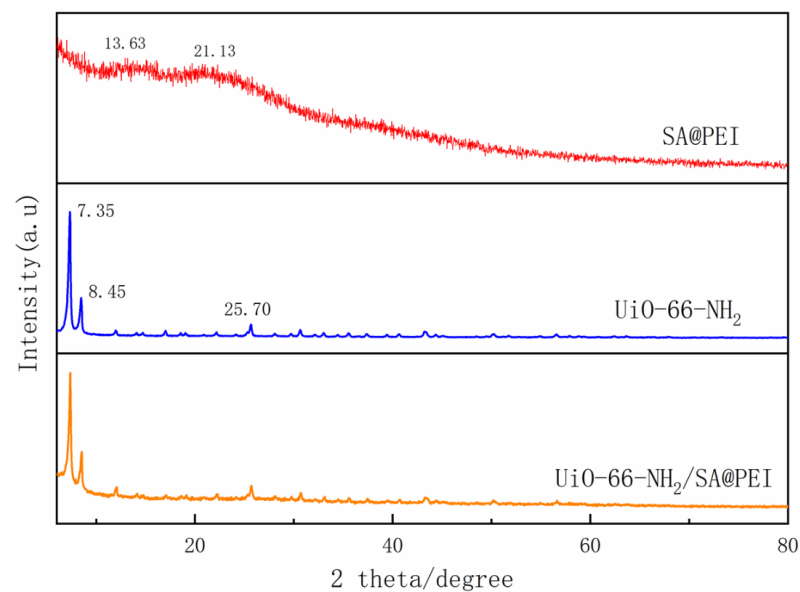


Figure 4. XRD patterns of SA@PEI, UiO-66-NH₂ and UiO-66-NH₂/SA@PEI.

3.2. The Adsorption Capacity of UiO-66-NH₂/SA@PEI under Different Conditions

In order to determine the phosphate adsorption capacity of UiO-66-NH₂/SA@PEI from water, experiments were conducted under various conditions, including pH, temperature, adsorbent quantity, and initial phosphate concentration. To investigate the impact of pH on adsorption capacity, the pH was varied from 1 to 9 using 0.05 g of adsorbent, an initial phosphate concentration of 100 mg/L, a volume of 12.5 mL, and an adsorption temperature of 25 °C. Figure 5a illustrates the consistently high adsorption capacity of UiO-66-NH₂/SA@PEI for phosphate across the pH range of 1–9. The positively charged surface of UiO-66-NH₂ at lower pH levels enhanced its affinity for negatively charged H₂PO₄⁻/HPO₄²⁻, while the protonation of -NH₂ to -NH₃⁺ further strengthened the electrostatic adsorption of phosphate ions.

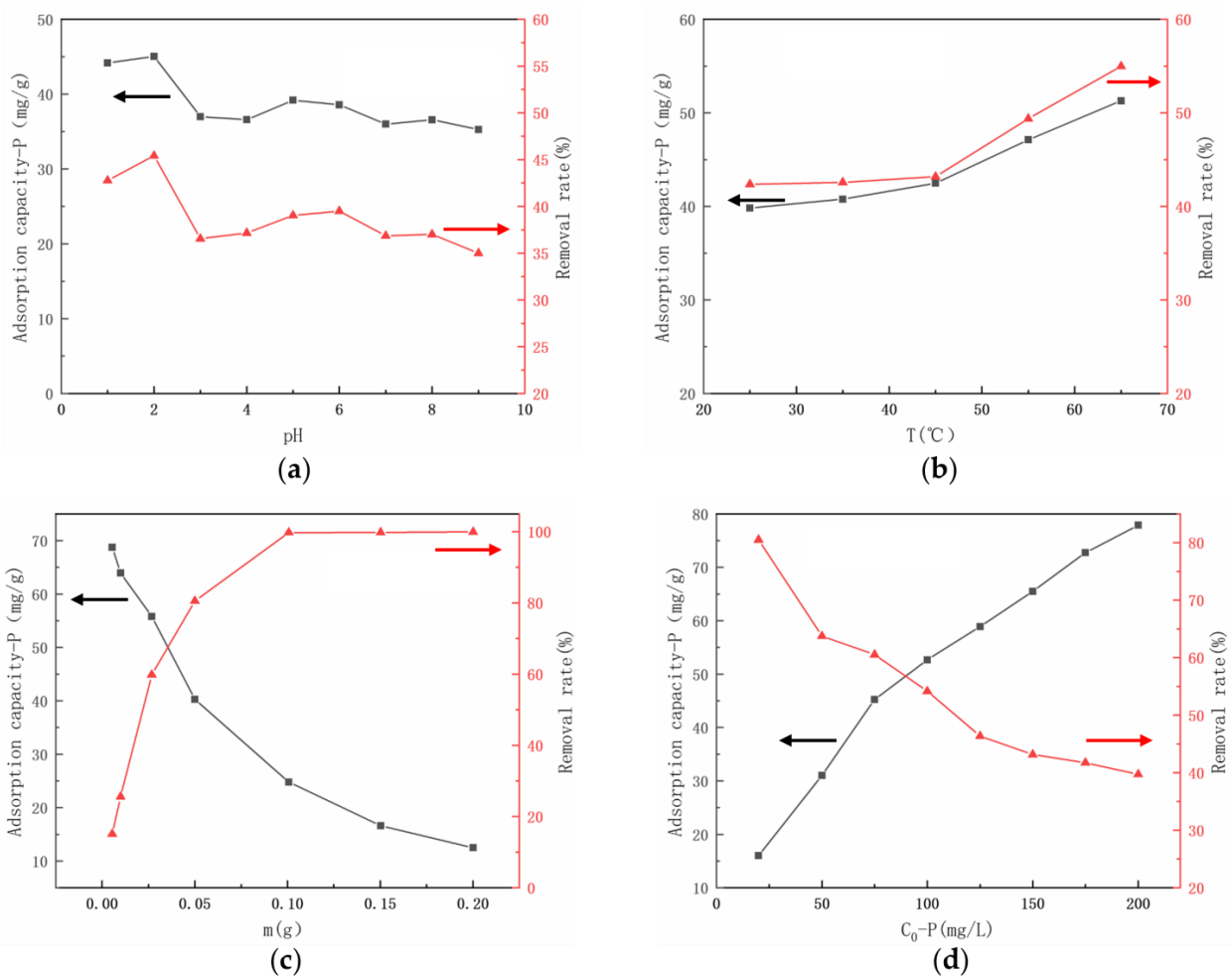


Figure 5. The adsorption capacity and removal rate of the phosphate adsorption by UiO-66-NH₂/SA@PEI under different conditions: (a) pH, (b) temperature, (c) dosage of adsorbent (d) initial phosphate concentration.

Adsorption experiments were conducted at temperatures of 25 °C, 35 °C, 45 °C, 55 °C, and 65 °C using a dosage of 0.05 g of UiO-66-NH₂/SA@PEI, a phosphate concentration of 100 mg/L, a pH of 2, and a volume of 12.5 mL. Figure 5b depicts the relationship between the adsorption capacity, removal rate, and temperature of phosphate adsorbed by UiO-66-NH₂/SA@PEI. The results indicated a direct correlation between temperature and the adsorption capacity of phosphate by the adsorbent, increasing from 39.8 mg/g to 51.3 mg/g. Additionally, the removal rate rose from 42.4% to 55.1%. These findings suggest that the adsorption of phosphate by UiO-66-NH₂/SA@PEI is an endothermic process, as higher temperatures enhanced the adsorption capacity.

The effect of varying amounts of adsorbent on phosphate removal was examined using an initial phosphate solution of 100 mg/L, a 25 mL volume, a pH of 2, and a temperature of 65 °C. Different dosages of adsorbent—0.0055 g, 0.01 g, 0.0265 g, 0.05 g, 0.1 g, 0.15 g, and 0.2 g—were employed in the investigation. As shown in Figure 5c, upon increasing the dosage of UiO-66-NH₂/SA@PEI, the adsorption capacity of the adsorbent reached 68.75 mg/g at a dosage of 0.0055 g. Increasing the dosage of the adsorbent led to an increase in adsorption sites; however, the phosphate content in the system remained constant, resulting in internal competition within the adsorbent. This competition led to a decrease in the amount of phosphate adsorbed per unit of adsorbent, hence reducing the adsorption capacity. The removal efficiency of UiO-66-NH₂/SA@PEI for phosphorus initially increased rapidly, then plateaued. At a dosage of 0.1 g, the removal efficiency of UiO-66-NH₂/SA@PEI in the adsorption system reached 99.76%. Beyond a dosage of 0.1 g, the removal efficiency remained relatively constant, indicating an excess of adsorption sites in the adsorbent compared to the phosphate content in the system.

An investigation into the effect of initial concentration on the removal of P using UiO-66-NH₂/SA@PEI (a dosage of 0.05 g, a pH of 2, a volume of 12.5 mL, and an adsorption temperature of 65 °C) revealed that the adsorption amount increased with an increase in the initial concentration (Figure 5d). However, the rate of increase in the adsorption amount decreased with a higher initial concentration, resulting in a decrease in the removal rate of the adsorbent [36]. Higher initial concentrations led to an increase in adsorption capacity, with the rate of increase gradually decreasing. However, higher initial concentrations also reduced the removal efficiency of the adsorbent. The high initial phosphate concentrations facilitated the binding of phosphate ions to the adsorption sites on UiO-66-NH₂/SA@PEI. As the number of adsorption sites was limited once saturation was reached, no further adsorption occurred. Consequently, higher initial concentrations resulted in lower phosphate removal rates.

3.3. Adsorption Kinetics of Phosphate by UiO-66-NH₂/SA@PEI

To investigate the adsorption kinetics of phosphate on UiO-66-NH₂/SA@PEI, kinetic data were fitted using pseudo-first-order (3), pseudo-second-order (4), and Elovich (5) models with varying initial phosphate concentrations.

$$Q_t = Q_e \left(1 - e^{-k_1 t}\right) \quad (3)$$

$$Q_t = k_2 Q_e^2 t / (1 + k_2 Q_e t) \quad (4)$$

$$Q_t = [\ln(\alpha\beta) + \ln t] / \beta \quad (5)$$

Q_t is the adsorption amount of UiO-66-NH₂/SA@PEI at time t , mg-P/g; Q_e is the adsorption amount at adsorption equilibrium, mg-P/g; k is the adsorption constant of each model, k_1 -h⁻¹, k_2 -g/(mg·h); α is the adsorption rate constant, mg/(mg·h); and β is the adsorbent surface coverage and chemical adsorption activation of energy-related parameters, g/mg.

The curve fitting for the adsorption kinetic data of UiO-66-NH₂/SA@PEI on phosphate is illustrated in Figure 6, with corresponding fitting parameters detailed in Table 1. The correlation coefficients of the pseudo-first-order and pseudo-second-order kinetic models at initial concentrations of 20 mg/L, 50 mg/L, and 100 mg/L exceeded 0.99, indicating a strong correlation. Notably, the pseudo-second-order kinetic model showed a higher coefficient of determination compared to the pseudo-first-order kinetic model, suggesting that the adsorption process was primarily governed by chemical adsorption. Phosphate was effectively adsorbed onto the materials through a chemical reaction, also as evidenced by the emergence of a peak at 1047 cm⁻¹, corresponding to the P-O stretching vibration peak following phosphate adsorption in the FTIR spectrum (Figure 2d).

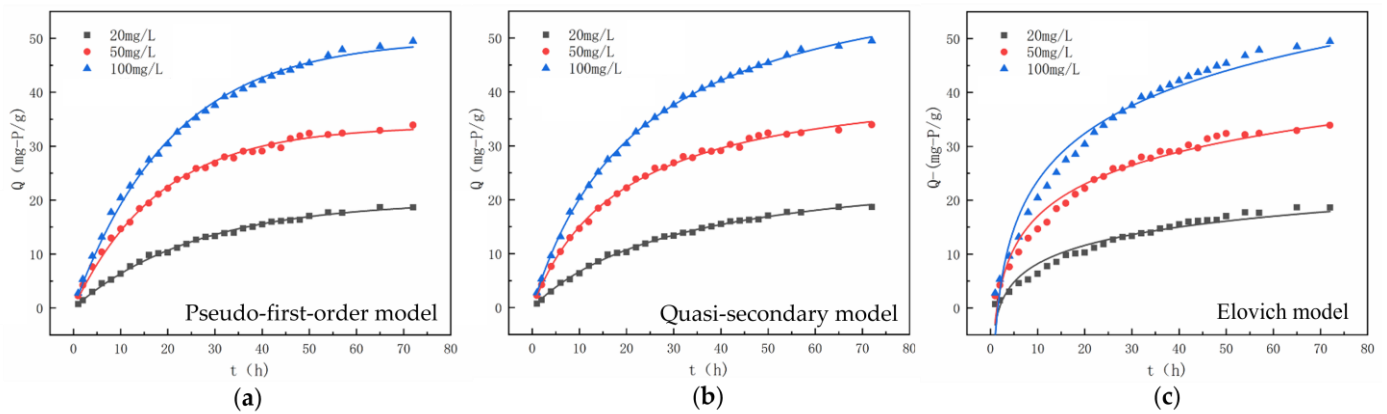


Figure 6. Model fitting curves for phosphate adsorption by UiO-66-NH₂/SA@PEI, (a) Pseudo-first-order model, (b) Quasi-secondary model and (c) Elovich model.

Table 1. Fitting parameters of the kinetic model of UiO-66-NH₂/SA@PEI for phosphate adsorption.

Kinetic Model		Initial Concentration of Phosphate Solution (mg/L)		
		20	50	100
Pseudo-first-order model	k_1	0.03877	0.05502	0.04844
	Q_e	19.7897	33.7230	49.9256
	R^2	0.9970	0.9959	0.9971
Quasi-secondary model	k_2	0.00117	0.0012	0.00066
	Q_e	27.4322	43.6677	66.1599
	R^2	0.9978	0.9973	0.9993
Elovich model	α	2.6000	6.2009	8.1156
	β	0.2031	0.1160	0.0787
	R^2	0.9472	0.9701	0.9654

3.4. The Adsorption Isotherm of Phosphate by UiO-66-NH₂/SA@PEI

The adsorption isotherm, illustrating the equilibrium concentration (C_e) and adsorbed amount (Q_e) at a given temperature and pH, was analyzed using the Langmuir (6), Freundlich (7), Temkin (8), and Dubinin–Radushkevich (DR) (9) models. The formulas, associated parameters, and fitting curves for these models are presented in Table 2 and Figure 7.

$$Q_e = Q_m K_L C_e / (1 + K_L C_e) \tag{6}$$

$$Q_e = K_F C_e^{1/n_F} \tag{7}$$

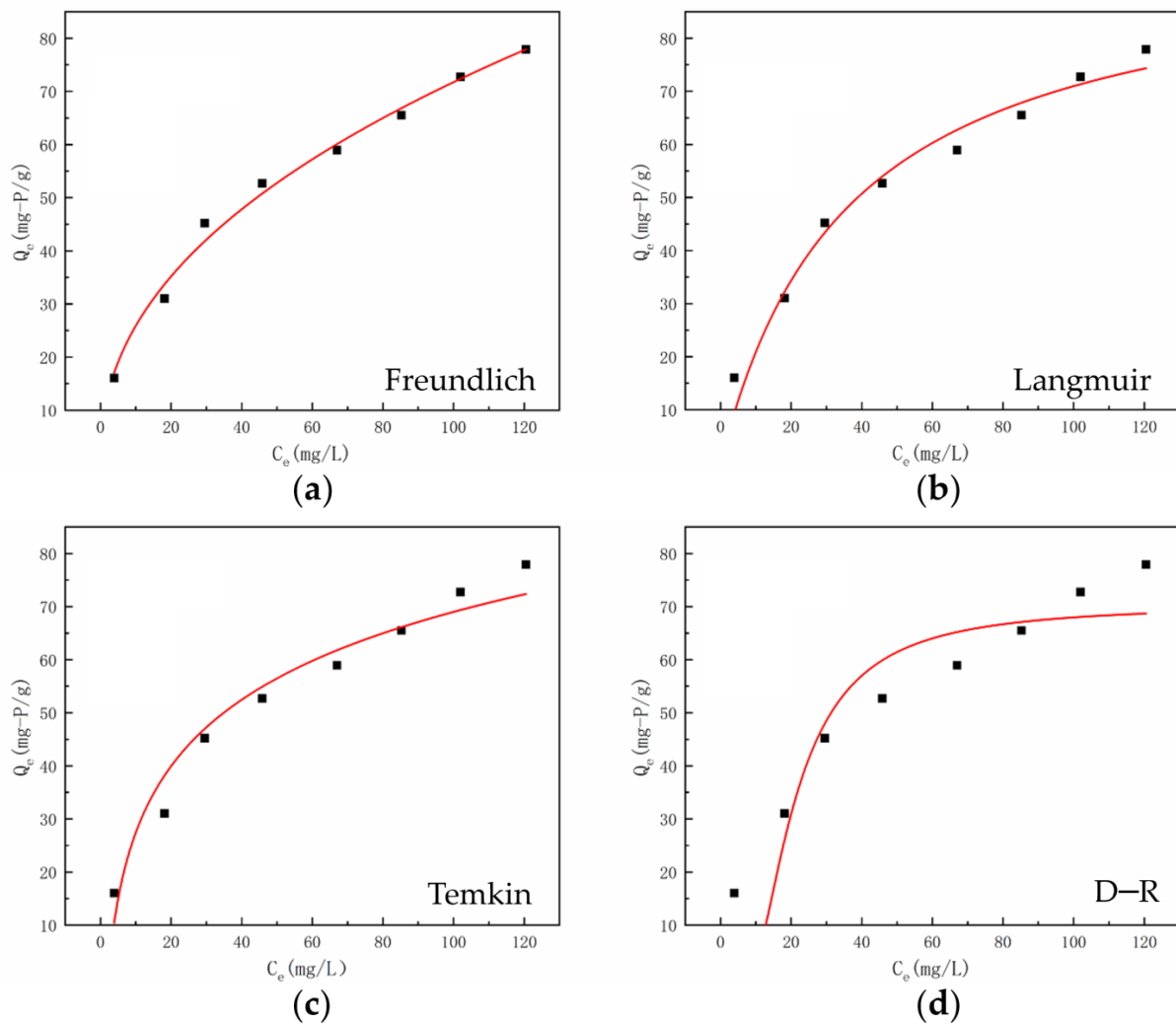
$$Q_e = B \ln K_T + B \ln C_e \tag{8}$$

$$Q_e = Q_m \exp \left\{ -K_D \left[RT \ln \left(1 + \frac{1}{C_e} \right) \right]^2 \right\} \tag{9}$$

Q_e is the adsorption amount at adsorption equilibrium, mg-P/g; K is the adsorption constant of each model, K_L -L/mg, K_F -mg/g, K_T -L/mg, and K_D -mol²/kJ²; Q_m is the theoretical maximum adsorption capacity, mg-P/g; n_F is the Freundlich model constant, which is related to the adsorption strength; B is the Temkin model constant related to the heat of adsorption, kJ/mol; C_e is the concentration at equilibrium, mg/L; R is the ideal gas constant, 8.314 kJ/mol/K; and T is the absolute temperature, K.

Table 2. Adsorption isotherm model fitting parameters of UiO-66-NH₂/SA@PEI.

Langmuir model	Q_m	K_L	R^2
	96.7882	0.0275	0.9680
Freundlich model	K_F	$1/n_F$	R^2
	9.3226	0.4431	0.9901
Temkin model	K_T	B	R^2
	0.4552	18.0698	0.9470
D–R model	Q_m	K_D	R^2
	70.3320	2.3737×10^{-5}	0.8157

**Figure 7.** The adsorption isotherm of phosphate by UiO-66-NH₂/SA@PEI, (a) Freundlich model, (b) Langmuir model, (c) Temkin model and (d) D–R model.

As shown in Table 2 and Figure 7, the adsorption isotherms of UiO-66-NH₂/SA@PEI were analyzed using the Langmuir, Freundlich, Temkin, and Dubinin–Radushkevich models. The correlation coefficients (R^2) for the Langmuir, Freundlich, and Temkin models were all above 0.9, indicating strong correlations [37]. However, the Dubinin–Radushkevich model had an R^2 of only 0.8157, making it unsuitable for data fitting. The Langmuir model predicted a maximum theoretical adsorption capacity (Q_m) of 96.8 mg/g for P on UiO-66-NH₂/SA@PEI. The Freundlich model exhibited the highest correlation coefficient ($R^2 = 0.9901$) compared to the Langmuir ($R^2 = 0.9680$) and Temkin ($R^2 = 0.94701$) models,

suggesting non-uniform surface adsorption. The adsorption data demonstrated a good fit with the Freundlich model, showing a $1/n_F$ value of 0.4431, which is below 0.5. This value indicates the presence of chemical adsorption between phosphate and the adsorbent, highlighting the ease of phosphate adsorption. The Temkin model showed a strong correlation, implying a significant role of electrostatic forces in the adsorption process.

3.5. Cyclic Adsorption Performance of UiO-66-NH₂/SA@PEI

An experiment was conducted to assess the cyclic adsorption capacity of UiO-66-NH₂/SA@PEI following regeneration, utilizing NaOH for desorption. Re-adsorption took place under consistent initial phosphate concentration, adsorption temperature, and pH conditions. After five cycles, the removal rate still reached 99%, indicating that UiO-66-NH₂/SA@PEI has a good cyclic adsorption capacity as a phosphate adsorbent (Figure 8).

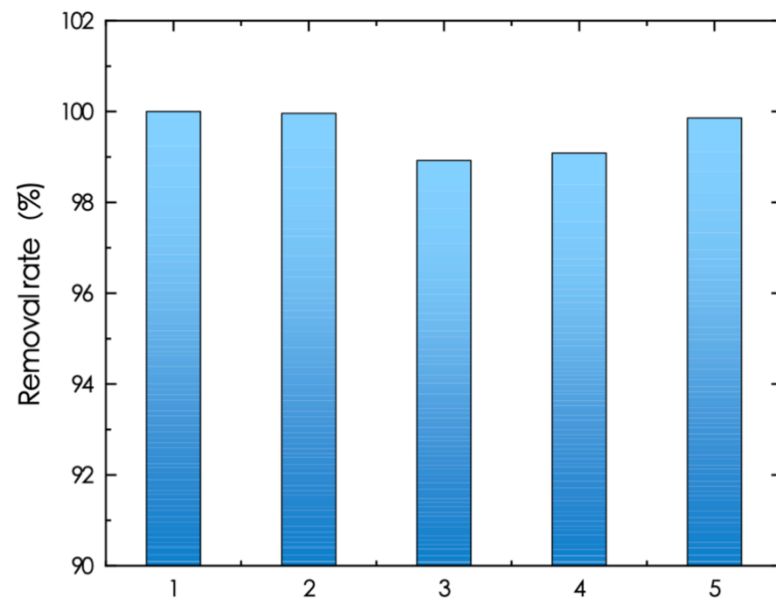


Figure 8. Cyclic adsorption performance of UiO-66-NH₂/SA@PEI.

3.6. Dynamic Adsorption Capacity

To further examine the dynamic adsorption capacity of UiO-66-NH₂/SA@PEI, experiments were conducted at different initial concentrations and flow rates. As depicted in Figure 9, a phosphate solution was delivered into a fixed-bed column containing UiO-66-NH₂/SA@PEI, using a peristaltic pump for dynamic adsorption under various conditions.

The Thomas model (10) was used to fit the results of the experiments. The removal rate of phosphate was calculated by Formula (11).

$$\frac{C_t}{C_0} = \frac{1}{1 + e^{\frac{K_T Q m}{v} - K_T C_0 t}} \quad (10)$$

$$R \% = \frac{C_0 v t_e / 1000}{\frac{v}{1000} \int_0^{t_e} (C_0 - C_t) dt} \times 100\% \quad (11)$$

C_0 is the initial concentration of the inlet water, mg-P/L; C_t is the outlet solution concentration at time t , mg-P/L; K_T is the Thomas model constant, mL/(min·mg); v is the flow rate of the solution, mL/min; Q is the adsorption capacity of the adsorbent, mg-P/g; m is the mass of the adsorbent, g; R (%) is the removal rate; and the depletion point t_e (min) of the adsorption column is the time point when $C_t/C_0 = 95\%$.

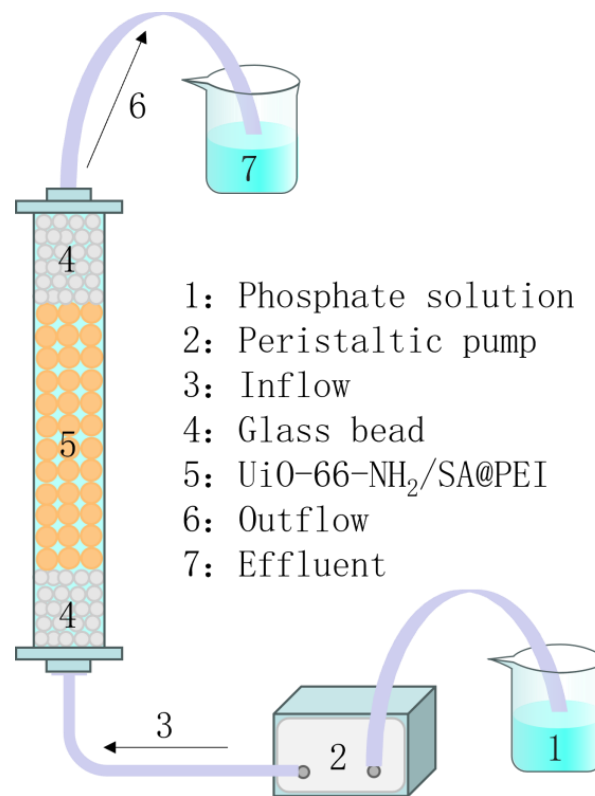


Figure 9. Schematic diagram of fixed-bed column used in dynamic adsorption study of phosphate onto UiO-66-NH₂/SA@PEI.

The Thomas model was used to fit the adsorption data of UiO-66-NH₂/SA@PEI with a dosage of 2 g, initial concentrations of 50 mg/L and 100 mg/L and water inlet rates of 1 mL/min and 2 mL/min, respectively. The results showed that the correlation coefficient R^2 fitted by the model was greater than 0.95, indicating a strong correlation (Table 3, Figure 10). According to the Thomas model, it can be seen that as the flow rate increased, the adsorption capacity decreased and the rate constant (K_T) increased, suggesting that a lower flow rate is more conducive to adsorption. This is because a lower flow rate will increase the contact time between the adsorbent and the solution, thus improving the adsorption effect and increasing the rate constant. Additionally, as the initial concentration increased, the adsorption capacity decreased and the rate constant increased. This is because a higher concentration increases the concentration difference between the liquid and the adsorbent, thus increasing the driving force transmitted to it. At the same time, the high concentration occupies the adsorption sites faster, resulting in a decrease in the rate constant and a decrease in the t_e .

Table 3. Thomas model for dynamic adsorption capacity of UiO-66-NH₂/SA@PEI under different conditions.

C_0	v	m	t_e	R	Thomas Model		
					K_T	Q	R^2
50	1	2	291	29.19	0.2531	1.4594	0.9951
50	2	2	182	26.54	0.3830	1.3494	0.9873
100	2	2	89	23.79	0.4622	1.1422	0.9896

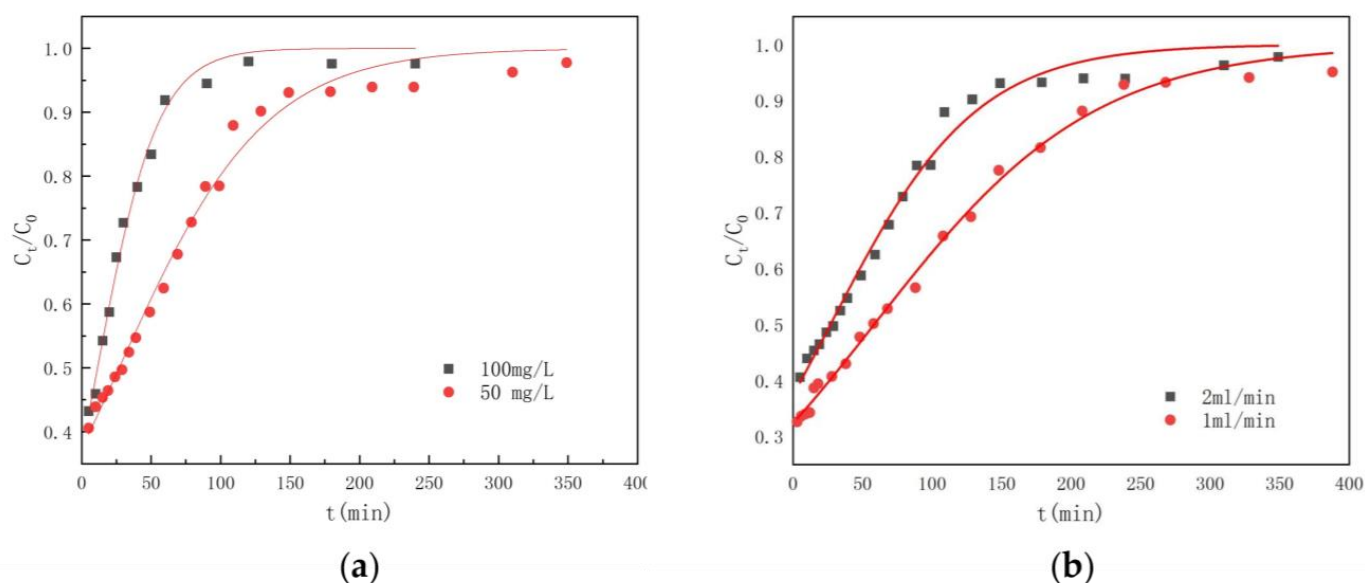


Figure 10. Thomas model fitting for dynamic adsorption capacity of UiO-66-NH₂/SA@PEI under different conditions, (a) initial phosphate concentration and (b) water inlet rate.

3.7. Phosphate Adsorption Mechanism

The adsorption mechanism of UiO-66-NH₂/SA@PEI involves numerous metal sites, with Zr present in the form of Zr₆O₄(OH)₄ carrying a positive charge. This allows for electrostatic interactions with negatively charged phosphate ions. At low pH, the -OH groups on Zr₆O₄(OH)₄ are more reactive, enabling phosphate ions to adsorb by displacing -OH groups on Zr [38]. Additionally, UiO-66-NH₂/SA@PEI provides another adsorption site through positively charged amine groups on UiO-66-NH₂ and PEI, which interact electrostatically with phosphate ions for adsorption [12]. In UiO-66-NH₂/SA@PEI material, the predominant adsorption sites exposed to the solvent are zirconium metal and amino groups. The presence of water is essential for the adsorption process. When the adsorbent input is equal, environments rich in water facilitate full accessibility of the adsorption sites to the solvent, thereby enhancing the adsorption capacities and accelerating saturation attainment [39].

The composite porous structure of UiO-66-NH₂/SA@PEI enhances phosphate mass transfer and diffusion within its pores, thereby increasing adsorption capacity on the UiO-66-NH₂ surface. Despite not having the highest specific surface area, the UiO-66-NH₂/SA@PEI prepared in this study exhibited superior adsorption capacity due to its porosity and improved particle dispersion, resulting in a greater number of available adsorption sites, as illustrated in Table 4.

Table 4. The phosphate adsorption capacities with different porous materials.

Materials	Specific Surface Area (m ² /g)	Pore Size (nm)	Adsorption Capacity (mg/g)	Ref.
UiO-66	990	—	27.70	[39]
UiO-66-NH ₂	815	—	30.00	
MFC@UiO-66	—	—	7.83	[40]
Mg-doped UiO-66-NH ₂	397	1.96	68.00	[41]
Ce-doping UiO-66-NH ₂	557.7	1.96	69.10	[42]
UiO-66-NH ₂ /SA@PEI	325.1	3.7	68.75	This work

4. Conclusions

A UiO-66-NH₂/SA@PEI composite material was synthesized for phosphate adsorption. After the formation of the composite materials, the UiO-66-NH₂ nanoparticles ex-

hibited good dispersibility and a close association with the SA network. This composite material not only protected and stabilized UiO-66-NH₂ but also resolved the issue of recyclability inherent in UiO-66-NH₂ as an adsorbent. With a high concentration of Zr metal sites and amino active sites, the composite material demonstrated efficient adsorption of phosphate ions in aqueous solutions. Under optimal conditions of 65 °C and pH = 2, 0.05 g UiO-66-NH₂/SA@PEI achieved an adsorption of 68.75 mg/g, and the adsorption rate remained at 99% after five cycles. The higher temperature favored adsorption, indicating an endothermic reaction. Data fitting revealed that the pseudo-second-order and Freundlich models best matched the experimental results. The cyclic adsorption tests demonstrated UiO-66-NH₂/SA@PEI's strong re-adsorption capability, highlighting its potential as a phosphate adsorbent.

Author Contributions: Conceptualization, X.L. and F.D.; methodology, X.L. and F.D.; software, X.L.; formal analysis, X.L. and F.D.; investigation, X.L.; resources, X.L.; data curation, X.L. and F.D.; writing—original draft preparation, X.L., Y.X. and F.D.; writing—review and editing, X.L., Y.X. and F.D.; supervision, F.D.; project administration, Y.X. and F.D.; funding acquisition, Y.X. All authors have read and agreed to the published version of the manuscript.

Funding: This research was funded by the National Natural Science Foundation of China (52063006).

Data Availability Statement: Data is contained within the article.

Conflicts of Interest: The authors declare no conflicts of interest.

References

1. Maharajan, T.; Ceasar, S.A.; Krishna, T.P.A.; Ignacimuthu, S. Management of phosphorus nutrient amid climate change for sustainable agriculture. *J. Environ. Qual.* **2021**, *50*, 1303–1324. [[CrossRef](#)] [[PubMed](#)]
2. Gu, Y.; Xie, D.; Ma, Y.; Qin, W.; Zhang, H.; Wang, G.; Zhang, Y.; Zhao, H. Size Modulation of Zirconium-Based Metal Organic Frameworks for Highly Efficient Phosphate Remediation. *ACS Appl. Mater. Interfaces* **2017**, *9*, 32151–32160. [[CrossRef](#)] [[PubMed](#)]
3. Zhan, T.R.; Zhang, Y.M.; Yang, Q.; Deng, H.H.; Xu, J.; Hou, W.G. Ultrathin layered double hydroxide nanosheets prepared from a water-in-ionic liquid surfactant-free microemulsion for phosphate removal from aquatic systems. *Chem. Eng. J.* **2016**, *302*, 459–465. [[CrossRef](#)]
4. Zahed, M.A.; Salehi, S.; Tabari, Y.; Farraji, H.; Ataei-Kachoei, S.; Zinatizadeh, A.A.; Kamali, N.; Mahjouri, M. Phosphorus removal and recovery: State of the science and challenges. *Environ. Sci. Pollut. Res.* **2022**, *29*, 58561–58589. [[CrossRef](#)] [[PubMed](#)]
5. Priya, E.; Kumar, S.; Verma, C.; Sarkar, S.; Maji, P.K. A comprehensive review on technological advances of adsorption for removing nitrate and phosphate from waste water. *J. Water Process Eng.* **2022**, *49*, 103159. [[CrossRef](#)]
6. Wang, X.Q.; Doug, L.; Li, Z.L.; Yang, L.; Yu, J.Y.; Ding, B. Flexible Hierarchical ZrO₂ Nanoparticle-Embedded SiO₂ Nanofibrous Membrane as a Versatile Tool for Efficient Removal of Phosphate. *ACS Appl. Mater. Interfaces* **2016**, *8*, 34668–34676. [[CrossRef](#)]
7. Qiu, H.; Liang, C.; Yu, J.H.; Zhang, Q.R.; Song, M.X.; Chen, F.H. Preferable phosphate sequestration by nano-La(III) (hydr)oxides modified wheat straw with excellent properties in regeneration. *Chem. Eng. J.* **2017**, *315*, 345–354. [[CrossRef](#)]
8. Liu, X.; Shen, F.; Smith, R.L., Jr.; Qi, X. Black liquor-derived calcium-activated biochar for recovery of phosphate from aqueous solutions. *Bioresour. Technol.* **2019**, *294*, 122198. [[CrossRef](#)]
9. Lin, X.; Xie, Y.; Lu, H.; Xin, Y.; Altaf, R.; Zhu, S.; Liu, D. Facile preparation of dual La-Zr modified magnetite adsorbents for efficient and selective phosphorus recovery. *Chem. Eng. J.* **2020**, *413*, 127530. [[CrossRef](#)]
10. Alrebdi, T.A.; Ahmed, H.A.; Alrefaee, S.H.; Pashameah, R.A.; Toghan, A.; Mostafa, A.M.; Alkallas, F.H.; Rezk, R.A. Enhanced adsorption removal of phosphate from water by Ag-doped PVA-NiO nanocomposite prepared by pulsed laser ablation method. *J. Mater. Res. Technol. JmrT* **2022**, *20*, 4356–4364. [[CrossRef](#)]
11. He, Q.; Zhao, H.; Teng, Z.; Wang, Y.; Li, M.; Hoffmann, M.R. Phosphate removal and recovery by lanthanum-based adsorbents: A review for current advances. *Chemosphere* **2022**, *303*, 134987. [[CrossRef](#)] [[PubMed](#)]
12. Afridi, M.N.; Adil, S.; Byambaa, B.; Sohail, M.; Wang, J.; Li, C. Progress, challenges, and prospects of MOF-based adsorbents for phosphate recovery from wastewater. *J. Water Process Eng.* **2024**, *63*, 105530. [[CrossRef](#)]
13. Gutov, O.V.; Molina, S.; Escudero-Adan, E.C.; Shafir, A. Modulation by Amino Acids: Toward Superior Control in the Synthesis of Zirconium Metal-Organic Frameworks. *Chem. A Eur. J.* **2016**, *22*, 13582–13587. [[CrossRef](#)] [[PubMed](#)]
14. Liu, R.; Chi, L.; Wang, X.; Wang, Y.; Sui, Y.; Xie, T.; Arandiyana, H. Effective and selective adsorption of phosphate from aqueous solution via trivalent-metals-based amino-MIL-101 MOFs. *Chem. Eng. J.* **2019**, *357*, 159–168. [[CrossRef](#)]
15. Wu, J.; Zhou, J.; Zhang, S.; Alsaedi, A.; Hayat, T.; Li, J.; Song, Y. Efficient removal of metal contaminants by EDTA modified MOF from aqueous solutions. *J. Colloid Interface Sci.* **2019**, *555*, 403–412. [[CrossRef](#)] [[PubMed](#)]
16. Zhang, Q.; Sang, Z.; Li, Q.; Gong, J.; Peng, X.; Li, L.; Zhang, Z.; Zhang, B.; Li, S.; Yang, X. Facile fabrication of La/Ca bimetal-organic frameworks for economical and efficient remove phosphorus from water. *J. Mol. Liq.* **2022**, *356*, 119024. [[CrossRef](#)]

17. Cox, C.S.; Galicia, V.C.; Lessio, M. Computational Insights into As(V) Removal from Water by the UiO-66 Metal-Organic Framework. *J. Phys. Chem. C* **2021**, *125*, 3157–3168. [[CrossRef](#)]
18. Shams, M.; Dehghani, M.H.; Nabizadeh, R.; Mesdaghinia, A.; Alimohammadi, M.; Najafpoor, A.A. Adsorption of phosphorus from aqueous solution by cubic zeolitic imidazolate framework-8: Modeling, mechanical agitation versus sonication. *J. Mol. Liq.* **2016**, *224*, 151–157. [[CrossRef](#)]
19. Zhang, R.; Wang, Z.; Zhou, Z.; Li, D.; Wang, T.; Su, P.; Yang, Y. Highly Effective Removal of Pharmaceutical Compounds from Aqueous Solution by Magnetic Zr-Based MOFs Composites. *Ind. Eng. Chem. Res.* **2019**, *58*, 3876–3884. [[CrossRef](#)]
20. Assaad, N.; Sabeh, G.; Hmadeh, M. Defect Control in Zr-Based Metal-Organic Framework Nanoparticles for Arsenic Removal from Water. *ACS Appl. Nano Mater.* **2020**, *3*, 8997–9008. [[CrossRef](#)]
21. Sonal, S.; Mishra, B.K. A comprehensive review on the synthesis and performance of different zirconium-based adsorbents for the removal of various water contaminants. *Chem. Eng. J.* **2021**, *424*, 130509. [[CrossRef](#)]
22. Tao, Y.; Fang, F.; Lv, Q.; Qin, W.; He, X.; Zhang, Y.; Zhou, Y.; Li, X.; Li, J. Highly efficient removal of glyphosate from water by hierarchical-pore UiO-66: Selectivity and effects of natural water particles. *J. Environ. Manag.* **2022**, *316*, 115301. [[CrossRef](#)] [[PubMed](#)]
23. Gonzalez, L.; Gil-San-Millan, R.; Navarro, J.A.R.; Maldonado, C.R.; Barea, E.; Carmona, F.J. Green synthesis of zirconium MOF-808 for simultaneous phosphate recovery and organophosphorus pesticide detoxification in wastewater. *J. Mater. Chem. A* **2022**, *10*, 19606–19611. [[CrossRef](#)]
24. Wang, L.; Shi, C.; Pan, L.; Zhang, X.; Zou, J.-J. Rational design, synthesis, adsorption principles and applications of metal oxide adsorbents: A review. *Nanoscale* **2020**, *12*, 4790–4815. [[CrossRef](#)] [[PubMed](#)]
25. Valverde, A.; Payno, D.; Lezama, L.; Laza, J.M.; Wuttke, S.; de Luis, R.F. Multivariate Functionalization of UiO-66 for Photocatalytic Water Remediation. *Adv. Sustain. Syst.* **2022**, *6*, 2200024. [[CrossRef](#)]
26. Moumen, E.; Bazzi, L.; El Hankari, S. Metal-organic frameworks and their composites for the adsorption and sensing of phosphate. *Coord. Chem. Rev.* **2022**, *454*, 214376. [[CrossRef](#)]
27. Hosoya, K.; Ohtsuki, C.; Kawai, T.; Kamitakahara, M.; Ogata, S.-I.; Miyazaki, T.; Tanihara, M. A novel covalently crosslinked gel of alginate and silane with the ability to form bone-like apatite. *J. Biomed. Mater. Res. Part A* **2004**, *71*, 596–601. [[CrossRef](#)] [[PubMed](#)]
28. Xi, H.; Li, Q.; Yang, Y.; Zhang, J.; Guo, F.; Wang, X.; Xu, S.; Ruan, S. Highly effective removal of phosphate from complex water environment with porous Zr-bentonite alginate hydrogel beads: Facile synthesis and adsorption behavior study. *Appl. Clay Sci.* **2021**, *201*, 105919. [[CrossRef](#)]
29. Shan, S.; Tang, H.; Zhao, Y.; Wang, W.; Cui, F. Highly porous zirconium-crosslinked graphene oxide/alginate aerogel beads for enhanced phosphate removal. *Chem. Eng. J.* **2019**, *359*, 779–789. [[CrossRef](#)]
30. Zhao, Y.; Gai, L.; Liu, H.; An, Q.; Xiao, Z.; Zhai, S. Network interior and surface engineering of alginate-based beads using sorption affinity component for enhanced phosphate capture. *Int. J. Biol. Macromol.* **2020**, *162*, 301–309. [[CrossRef](#)]
31. Zeng, Z.; Sorescu, D.C.; White, D.L.; Hwang, S.I.; Shao, W.; He, X.; Schulte, Z.M.; Rosi, N.L.; Star, A. Heterogeneous Growth of UiO-66-NH₂ on Oxidized Single-Walled Carbon Nanotubes to form “Beads-on-a-String” Composites. *ACS Appl. Mater. Interfaces* **2021**, *13*, 15482–15489. [[CrossRef](#)]
32. Lozano-Vazquez, G.; Alvarez-Ramirez, J.; Lobato-Calleros, C.; Vernon-Carter, E.J.; Hernández-Marín, N.Y. Characterization of corn starch-calcium alginate xerogels by microscopy, thermal, XRD, and FTIR analyses. *Starch-Stärke* **2021**, *73*, 2000282. [[CrossRef](#)]
33. Paladini, G.; Venuti, V.; Crupi, V.; Majolino, D.; Fiorati, A.; Punta, C. FTIR-ATR analysis of the H-bond network of water in branched polyethyleneimine/TEMPO-oxidized cellulose nano-fiber xerogels. *Cellulose* **2020**, *27*, 8605–8618. [[CrossRef](#)]
34. Yang, J.; Dai, Y.; Zhu, X.; Wang, Z.; Li, Y.; Zhuang, Q.; Shi, J.; Gu, J. Metal-organic frameworks with inherent recognition sites for selective phosphate sensing through their coordination-induced fluorescence enhancement effect. *J. Mater. Chem. A* **2015**, *3*, 7445–7452. [[CrossRef](#)]
35. Strauss, I.; Chakarova, K.; Mundstock, A.; Mihaylov, M.; Hadjiivanov, K.; Guschanski, N.; Caro, J. UiO-66 and UiO-66-NH₂ based sensors: Dielectric and FTIR investigations on the effect of CO₂ adsorption. *Microporous Mesoporous Mater.* **2020**, *302*, 110227. [[CrossRef](#)]
36. Wang, L.; Wen, X.; Li, J.; Zeng, P.; Song, Y.; Yu, H. Roles of defects and linker exchange in phosphate adsorption on UiO-66 type metal organic frameworks: Influence of phosphate concentration. *Chem. Eng. J.* **2021**, *405*, 126681. [[CrossRef](#)]
37. Karim, K.H. Copper adsorption behavior in some calcareous soils using Langmuir, Freundlich, Temkin, and Dubinin-Radushkevich models. *J. Soil Sci. Agric. Eng.* **2020**, *11*, 27–34. [[CrossRef](#)]
38. Guan, T.; Li, X.; Fang, W.; Wu, D. Efficient removal of phosphate from acidified urine using UiO-66 metal-organic frameworks with varying functional groups. *Appl. Surf. Sci.* **2020**, *501*, 144074. [[CrossRef](#)]
39. Lin, K.-Y.A.; Chen, S.-Y.; Jochems, A.P. Zirconium-based metal organic frameworks: Highly selective adsorbents for removal of phosphate from water and urine. *Mater. Chem. Phys.* **2015**, *160*, 168–176. [[CrossRef](#)]
40. Liu, T.; Zheng, S.; Yang, L. Magnetic zirconium-based metal-organic frameworks for selective phosphate adsorption from water. *J. Colloid Interface Sci.* **2019**, *552*, 134–141. [[CrossRef](#)]

41. Afridi, M.N.; Kim, J.-O. Statistical optimization of Mg-doped UiO-66-NH₂ synthesis for resource recovery from wastewater using response surface methodology. *Appl. Surf. Sci.* **2022**, *606*, 154973. [[CrossRef](#)]
42. Liu, M.; Li, S.; Tang, N.; Wang, Y.; Yang, X.; Wang, S. Highly efficient capture of phosphate from water via cerium-doped metal-organic frameworks. *J. Clean. Prod.* **2020**, *265*, 121782. [[CrossRef](#)]

Disclaimer/Publisher's Note: The statements, opinions and data contained in all publications are solely those of the individual author(s) and contributor(s) and not of MDPI and/or the editor(s). MDPI and/or the editor(s) disclaim responsibility for any injury to people or property resulting from any ideas, methods, instructions or products referred to in the content.